

## GEOPHYSICS

# Oceanic plateau of the Hawaiian mantle plume head subducted to the uppermost lower mantle

Songqiao Shawn Wei<sup>1\*</sup>, Peter M. Shearer<sup>2</sup>, Carolina Lithgow-Bertelli<sup>3</sup>, Lars Stixrude<sup>3</sup>, Dongdong Tian<sup>1</sup>

The Hawaiian-Emperor seamount chain that includes the Hawaiian volcanoes was created by the Hawaiian mantle plume. Although the mantle plume hypothesis predicts an oceanic plateau produced by massive decompression melting during the initiation stage of the Hawaiian hot spot, the fate of this plateau is unclear. We discovered a megameter-scale portion of thickened oceanic crust in the uppermost lower mantle west of the Sea of Okhotsk by stacking seismic waveforms of SS precursors. We propose that this thick crust represents a major part of the oceanic plateau that was created by the Hawaiian plume head ~100 million years ago and subducted 20 million to 30 million years ago. Our discovery provides temporal and spatial clues of the early history of the Hawaiian plume for future plate reconstructions.

**E**arthquakes and volcanism at plate boundaries are well explained with the theory of plate tectonics, but explaining intraplate hot spot volcanoes requires the mantle plume hypothesis (1, 2). This hypothesis posits deep-rooted and relatively fixed plumes of hot material upwelling through the mantle from the deep Earth and accounts for the age-progressive surface expression known as the Hawaiian-Emperor seamount chain. As the Pacific Plate moves northwest (3, 4), the newest volcanoes are found in Hawaii to the southeast, and the oldest seamounts are near the Kamchatka-Aleutian trench junction in the northwest. The ~47 million year (Ma) bend of the seamount chain is usually attributed to a change in the Pacific Plate motion (5). The history of the Hawaiian-Emperor seamount chain is critical for understanding Earth's interior evolution and plate tectonics. In the classical view, a mantle plume consists of a large head (>2000 km across) and a thin tail (~200 km wide) (6). The plume head generates a large igneous province (LIP), such as the Ontong-Java oceanic plateau or the Deccan Traps. The plume tail creates an age-progressive intraplate volcanic chain. Several efforts have been made to associate ancient LIPs to hot spot volcanoes (7). For instance, the Deccan Traps are considered to result from the head of the Reunion mantle plume surfacing more than 68 Ma ago (8). However, because of the debatable early history of the Hawaiian-Emperor seamount chain, the fate of the Hawaiian mantle plume head and resulting oceanic plateau is unknown.

According to a variety of plate reconstructions (3, 4), the Hawaiian-Emperor seamount chain entered the Kamchatka subduction

zone. One proposal places this event as the cause of the cusp between the Kurile-Kamchatka and the Aleutian-Alaska trenches (9). The subduction of the seamounts generates arc lavas with geochemical signatures similar to oceanic island basalts on the Kamchatka Peninsula (10). The oldest surface portion of the Hawaiian-Emperor chain, the Meiji Guyot (older than 81 Ma) and Detroit Seamount (76 to 81 Ma) (11) are about to subduct into the Kamchatka Trench (Fig. 1). But whether the older parts of the seamount chain, particularly the plume head, also subducted into the deep mantle or stayed on Earth's surface is debated (12–14).

The fate of the Hawaiian plume head is critical to the origin of the mantle plume, which provides a temporal constraint on the longevity and persistence of chemical characteristics of Earth's deep mantle. Furthermore, the subduction of the expected oceanic plateau caused by the Hawaiian plume head may have changed plate motions. Niu *et al.* (12) proposed that the collision of this oceanic plateau with the Kamchatka Trench was responsible for the Pacific Plate reorientation that resulted in the 47-Ma bend in the Hawaiian-Emperor chain.

More importantly, the fate of this oceanic plateau is critical for understanding the role of oceanic plateaus in building continental lithosphere and in mantle convection. Owing to their excess crustal thickness and volume, oceanic plateaus are thought to be more difficult to subduct than individual seamounts (15). Because the Yakutat terrane southeast of Alaska is the only oceanic plateau that is currently undergoing subduction (16), whether oceanic plateaus were commonly subducted in the past is unclear. By analyzing ophiolitic basalts in Kamchatka, Portnyagin *et al.* (14) proposed that the Hawaiian plume head, or at least part of it, was accreted to the forearc of Kamchatka. This mechanism provides an important way to grow continental crust (7). In contrast, a seismic study of compressional-to-shear (*P*-to-*S*) waves converted at seismic discontinuities (receiver functions) in South

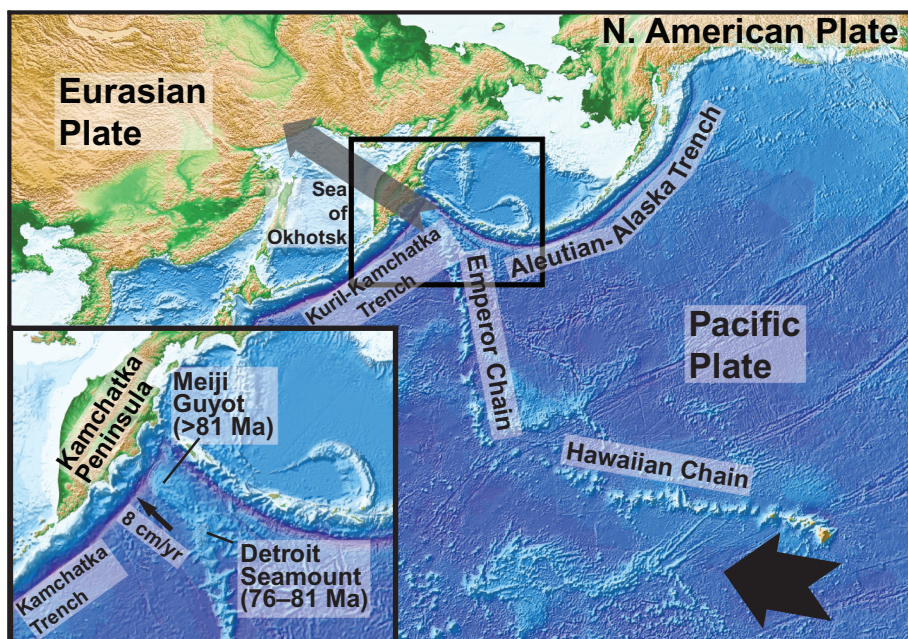


**Fig. 1. Topographic-bathymetric map (43) of the northern Pacific Ocean and Northeast Asia.** The bold black arrow indicates the current motion of the Pacific Plate at Hawaii relative to the Hawaiian plume, whereas the gray arrow represents the approximate trajectory of the Hawaiian-Emperor seamount chain into the Kamchatka subduction zone based on plate reconstructions (3, 4). Inset shows the Kamchatka region where the oldest seamounts (Meiji Guyot and Detroit Seamount) of the Hawaiian-Emperor chain are about to subduct into the Kamchatka Trench at a speed of 8 cm/year.

<sup>1</sup>Department of Earth and Environmental Sciences, Michigan State University, East Lansing, MI 48824, USA. <sup>2</sup>Cecil H. and Ida M. Green Institute of Geophysics and Planetary Physics, Scripps Institution of Oceanography, University of California, San Diego, La Jolla, CA 92093, USA. <sup>3</sup>Department of Earth, Planetary, and Space Sciences, University of California, Los Angeles, CA 90095, USA.

\*Corresponding author. Email: swei@msu.edu

America suggests that an oceanic plateau with a thickness of at least 13 to 19 km has subducted to ~100 km depth and is responsible for the Pampean flat slab (17). Geodynamic models also show that oceanic plateaus can subduct into the upper mantle, resulting in slowdown of subduction (18), formation of a flat slab (19), surface topography elevation (20), and dynamic uplift (21). In comparison with the subduction of normal oceanic crust of 6- to 7-km thickness, the input of thick oceanic plateaus might also change, at least locally, mantle composition and dynamics.

Although mantle plume conduits have been successfully imaged using seismic tomography with dense datasets (22), oceanic plateaus potentially subducted into the lower mantle have a 20- to 40-km crustal thickness that is smaller than the resolution in most tomographic studies. Owing to a lack of data, the tomography resolution in northeastern Siberia is particularly low in both global (23) and regional (24) images. Seismic reflected waves are more sensitive to sharp boundaries and provide a more effective tool to detect small-scale compositional heterogeneities in the deep mantle. Many seismic reflectors in the lower mantle have been imaged globally and attributed to segments of subducted crust (25–27). But ancient oceanic plateaus have

not been detected in the lower mantle, in part because of the limited data coverage in regions where they are expected.

We stacked SS precursors ( $SdS$ ) from 45 years of global seismic data to detect seismic reflectors in the lower mantle (28). The  $SdS$  seismic phase is the underside  $S$  wave reflection off the  $d$ -km discontinuity, which arrives before the surface-reflected SS phase (fig. S1A). Because SS precursors sample the midpoints between earthquakes and seismic stations, they provide good data coverage for remote regions and are widely used to image seismic discontinuities in the upper and mid-mantle (29). Besides the major seismic discontinuities extending globally, previous observations detected many smaller-scale reflectors using SS or  $PP$  precursors (26, 30).

We focus on a seismic reflector observed at ~810 km depth west of the Sea of Okhotsk, which was previously detected by limited data of  $PP$  precursors (30). The reflector has a width on the order of 1000 km and a depth varying from 780 to 820 km across (Fig. 2). When compared with global tomography models (23), the 810-km reflector appears to coincide with the Kamchatka slab, which is the ancient Pacific Plate subducted along the Kamchatka Trench (Fig. 3B). Given the limited resolution of to-

mography models, determining whether the reflector is at or above the slab surface (top interface) is challenging. The exact shape of this 810-km reflector is unclear because of the wide Fresnel zone (~1000 km across) and the low horizontal resolution of SS precursors. Additionally, determining the absolute reflector depth and topography relies on the seismic velocity in the upper mantle. With different three-dimensional (3D) mantle velocity models, the average depth of the 810-km reflector varies from 780 to 830 km depending on the choice of model, and its topography also changes from flat to elevated in the center by 30 km (figs. S2 and S3). The seismic signal  $S810S$  corresponding to the 810-km reflector has an apparent amplitude as strong as that of the  $S660S$  signal for the 660-km discontinuity. The absolute amplitude of  $S810S$  is influenced by incoherent stacking and seismic attenuation effects that are difficult to constrain (28). Therefore, we conclude that this megameter-scale reflector marks an  $S$ -wave impedance (product of density and  $S$ -wave velocity) increase at 780 to 820 km depths on the same order of magnitude of the impedance increase across the 660-km discontinuity.

In certain regions, we observe an azimuthal dependence of  $S810S$  in which the signal is only

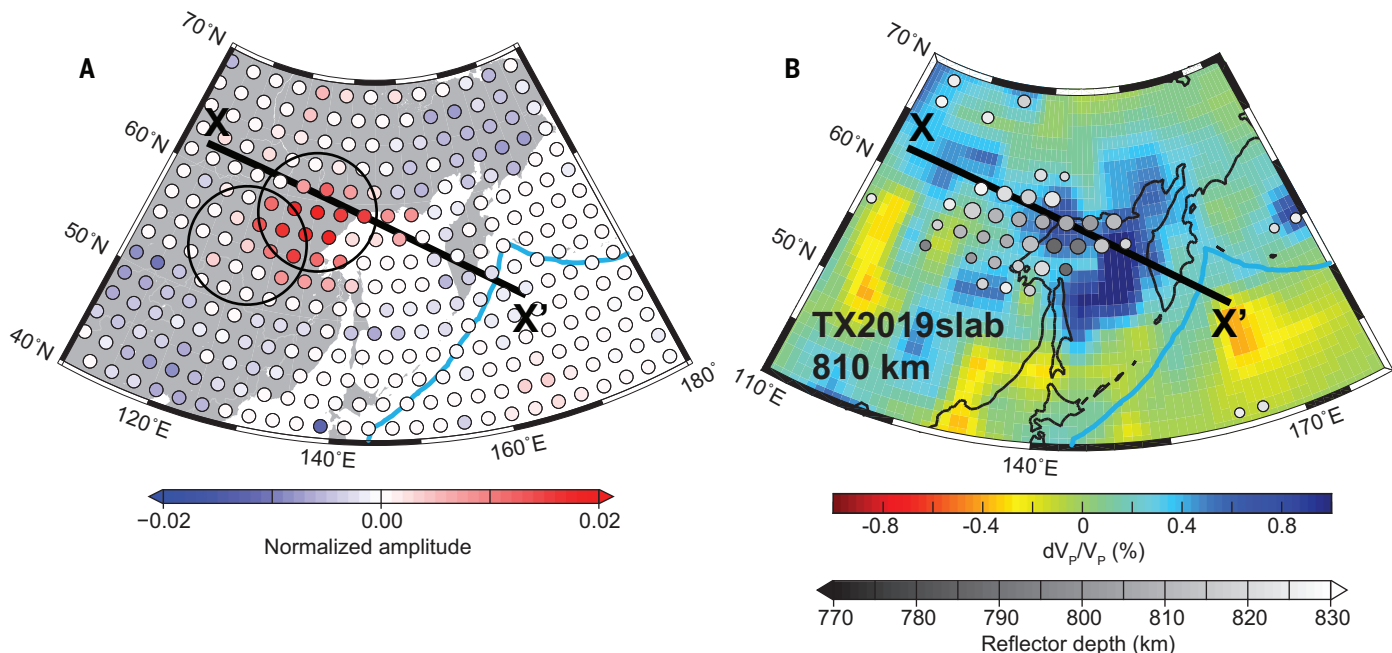


**Fig. 2. Maps of the 810-km reflector compared with velocity tomography.** (A) Map of amplitudes (above the 95% confidence level) of stacked SS precursor waveforms at 810 km depth in the Siberia-Okhotsk-Kamchatka region. The SS precursor amplitude is normalized to the SS amplitude in the same cap. Red circles show the high amplitude of  $S810S$ , indicating the 810-km reflector. SS precursors are stacked in overlapping bouncepoint caps of 5° radius and 2° spacing. The two large circles outline the actual area of caps, which are represented by small solid circles at their centers that are color-coded by amplitude. The lateral resolution of our data is ~1000 km, which is comparable to the size of each cap and the Fresnel zone width. The black line indicates the cross section X-X' in Fig. 3. The blue curves illustrate convergent plate boundaries (44). (B) Depth of the 810-km reflector in caps superimposed on the TX2019slab  $P$ -wave tomography model (23) at 810 km depth.  $dV_p/V_p$ , fractional  $P$ -wave velocity perturbation. The reflector depth is shown by the grayscale in caps where it is detected. Circle sizes are scaled to indicate the depth uncertainty, such that larger circles have lower uncertainties. In caps where the 810-km reflector is less evident owing to low amplitude, its depth has larger uncertainties. Caps with depth uncertainties greater than 10 km are omitted.

the size of each cap and the Fresnel zone width. The black line indicates the cross section X-X' in Fig. 3. The blue curves illustrate convergent plate boundaries (44). (B) Depth of the 810-km reflector in caps superimposed on the TX2019slab  $P$ -wave tomography model (23) at 810 km depth.  $dV_p/V_p$ , fractional  $P$ -wave velocity perturbation. The reflector depth is shown by the grayscale in caps where it is detected. Circle sizes are scaled to indicate the depth uncertainty, such that larger circles have lower uncertainties. In caps where the 810-km reflector is less evident owing to low amplitude, its depth has larger uncertainties. Caps with depth uncertainties greater than 10 km are omitted.

detectable along certain azimuths (fig. S4A). This dependence raises the question of whether the *S810S* signal is caused by near-source or near-receiver structures rather than a reflector beneath the midpoints (31). However, tests of this possibility confirm the existence of the 810-km reflector west of the Sea of Okhotsk, partly because our observation results from thousands of seismograms with a variety of focal mechanisms (28). Although 3D heterogeneity near sources or receivers may contaminate the *S810S* signals with *PPPS* and *PPPS* signals from the radial component, the energy contribution should be negligible because the similar *PS* and *PPS* waves are too weak to detect on the transverse component (fig. S5E). The azimuthal dependence may also suggest azimuthal anisotropy and small-scale heterogeneity that are difficult to determine conclusively given our limited data and resolution. Nevertheless, tests of possible scattering artifacts generated by distant 3D structures indicate that only a near-midpoint reflector is a plausible explanation for the *S810S* observations (28).

The 810-km reflector is surprising because it requires large and rapid increases in density and *S*-wave velocity. The surface of a flat and cold slab is a natural candidate to explain the reflector. Synthetic waveform modeling shows that either a moderately fast-velocity slab underneath a sub-660 low-velocity zone (LVZ) or a high-velocity slab is required to generate an *S810S* signal similar to our observation (fig. S6). By taking uncertainties of the *S810S* amplitude into account, conservative estimates lead to a 2% velocity reduction for the sub-660 LVZ or a 4% velocity increase within 5 km across the slab surface. However, neither the LVZ nor the ultra-high-velocity anomaly appears in any seismic tomography model, and we cannot explain either with thermal variations. In addition, the coherence of the *S810S* observations suggests that the 810-km reflector is nearly flat with a dip angle smaller than 2° within a megameter-wide area (figs. S7 and S8). Such a smooth and flat slab, although often a feature in conceptual models, is unlikely to be a realistic geometry in the mantle. For reference, the Pampean flat slab extends only ~300 km laterally at a depth of ~100 km before dipping into the deep Earth (77). Therefore, a simple slab model that is purely controlled by temperature cannot explain our observation.

This flat 810-km reflector could alternatively be caused by a pressure-dominated mineral phase transition. We used a thermodynamic simulation package called HeFESTo (32, 33) to calculate density and *S*-wave velocity profiles of mantle minerals for a variety of bulk compositions along various 1D thermal profiles (28). The mantle composition can be represented by pyrolite, a synthetic rock with the

chemical composition of the upper mantle that reaches equilibrium. On the other hand, the mantle is hypothesized as a mechanical mixture of two end-members of mantle differentiation, basalt and harzburgite, that never reaches equilibrium (34). With an identical bulk chemical composition, an equilibrium assemblage (pyrolite) and a mechanical mixture of basalt and harzburgite have different phase assemblages and therefore different mineralogical compositions and seismic velocities (34). A pyrolytic or harzburgite composition can produce a 660-km discontinuity corresponding to the olivine transition (ringwoodite to bridgemanite and ferropericlase) but with no obvious signal at ~810 km depth (fig. S9). In contrast, a basaltic composition can produce a strong

*S810S* signal corresponding to the garnet transition (majorite to bridgemanite) but a small *S660S* signal. If the mantle is a mechanical mixture of basalt and harzburgite, we expect to observe the olivine transition at ~660 km depth because of harzburgite, and the garnet transition at ~810 km depth because of the basaltic component. The predicted *S810S* signal is much weaker than the observation even if the basalt fraction (*f*) is 30%, which is much higher than the 18% fraction suggested for the entire mantle (34). Therefore, an equilibrium assemblage of pyrolytic composition or a mechanical mixture of basalt and harzburgite cannot explain the observed *S810S* signal.

A more realistic model is represented by a flat slab at 800 to 950 km depth with a basaltic

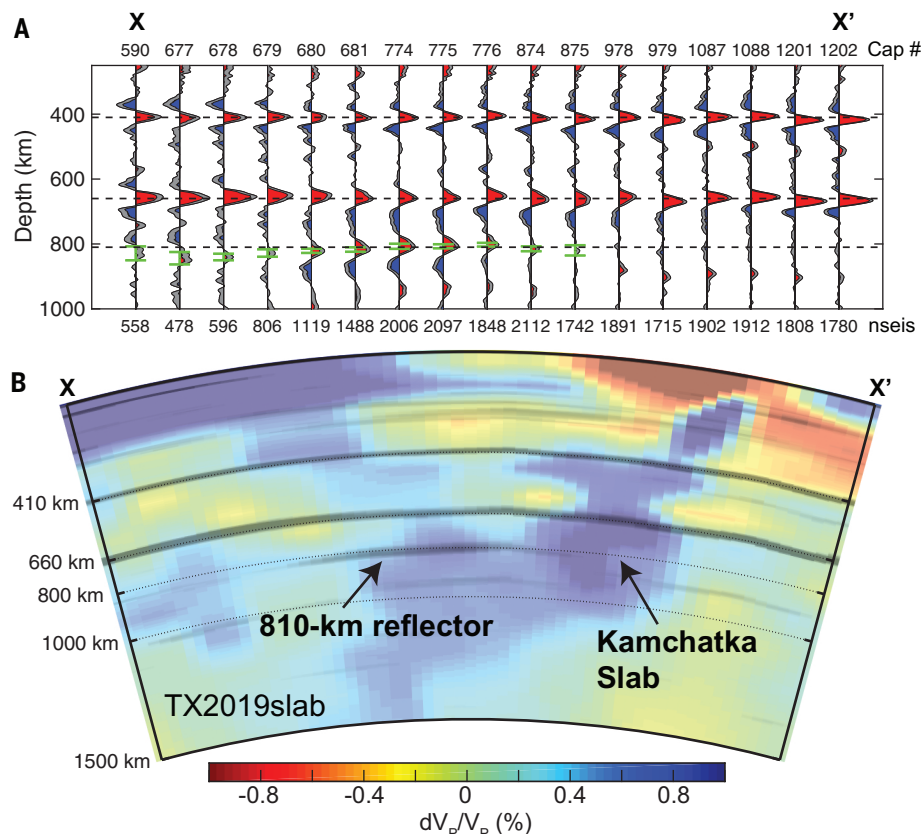


**Fig. 3. Cross section of apparent discontinuities and reflectors along the cross section shown in Fig. 2A.** (A) Stacked SS precursors observed in overlapping caps of 5° radius and 2° spacing. All seismograms are converted to the depth domain, stacked, and then corrected for 3D velocity heterogeneity using the TX2019slab S-wave velocity model (23). Red and blue indicate robust positive and negative signals above the 95% confidence levels, respectively, whereas gray shows the stack uncertainty ( $2\sigma$ ). Black dashed lines show depths of 410, 660, and 810 km. The cap indices (Cap #) are shown along the top, and the numbers of seismograms (nseis) stacked in those caps are shown along the bottom. A strong peak appears at ~810 km depth in certain caps. Green error bars indicate the depth of the 810-km reflector in each cap where it is detected. Weak positive signals at greater depths are artifacts resulting from interfering seismic phases (topside reflections off the 410- and 660-km discontinuities, that is, *Ss410s* and *Ss660s*, respectively) rather than SS precursors. Similar cross sections with different depth corrections based on other S-wave tomography models are shown in fig. S2. (B) Apparent discontinuities and reflectors (dark stripes) from SS precursor stacks superimposed on the TX2019slab P-wave tomography model (23). All positive signals shown in (A) are interpolated and shown as dark stripes, whereas all negative signals are omitted. Similar cross sections superimposed on other P-wave tomography models are shown in fig. S3.

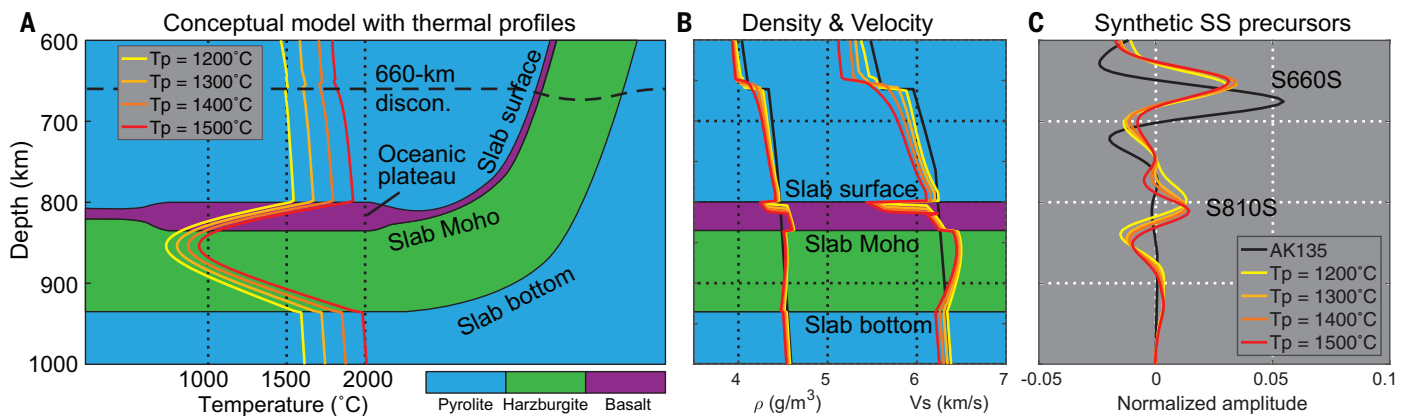


**Fig. 4. The garnet transition in an oceanic plateau in the lower mantle can explain the observed S810S signal.** (A) A conceptual model of the Kamchatka slab subducted into the lower mantle. Blue, green, and purple colors represent pyrolytic, harzburgite, and basaltic compositions, respectively. The oceanic plateau has a crustal thickness of 35 km, whereas the other parts of the oceanic crust are 6 km thick. Yellow to red curves show the thermal profiles across the flat slab with a variety of potential temperatures ( $T_p$ ). (B) Density ( $\rho$ ) and S-wave velocity ( $V_s$ ) profiles corresponding to the thermal profiles in (A). Black

curves indicate the AK135 reference model (45). The density profiles of the slab crust cross that of the reference model at 800 to 830 km depths owing to the majorite-bridgmanite transition, indicating that the oceanic crust is neutrally buoyant along all thermal profiles. (C) Synthetic SS precursor waveforms corresponding to the density and velocity profiles in (B). The S810S signal is strong enough to be observed along all thermal profiles. Note that we do not try to fit the exact waveform because of the large uncertainties of thermodynamic parameters of minerals and the S810S amplitude.

crust overriding on a depleted (harzburgite) slab mantle in the pyrolytic ambient mantle (35). Although seismic impedance decreases from the ambient mantle to the slab crust, it increases from the crust to the slab depleted mantle. More importantly, majorite garnet in the slab crust may transform to bridgmanite near 810 km depth, producing a sharp increase in seismic impedance (28). The impedance changes in a model with a normal crustal thickness of 6 km are not resolvable by long-period SS precursors with the vertical resolution of 30 to 50 km in the uppermost lower mantle (fig. S10A). In contrast, we obtain a strong S810S signal if we assume an oceanic plateau with a 35-km-thick crust, which is comparable to the crust of the Ontong-Java Plateau (36). This S810S signal results from the combination of all impedance changes from the slab surface to Moho (Fig. 4). If the oceanic plateau is 20 km thick, the S810S signal is still detectable, but with a weaker amplitude (fig. S10B). Furthermore, the density profile of the slab crust crosses that of the ambient mantle owing to the majorite-bridgmanite transition, suggesting that the slab crust, regardless of its thickness, is neutrally buoyant at the depths of 800 to 835 km. We cannot assess whether the slab crust has been detached from the downgoing slab mantle, as suggested by geodynamic models (37), because a model with an orphan slab crust can also produce a detectable S810S signal (fig. S10C). Nevertheless, the thick crust of the subducted oceanic plateau, roughly as wide as the Ontong-Java Plateau, probably has been floating in the mantle at 800 to 835 km depth since it reached these depths as a result of the neu-

tral buoyancy. This explains the large dimension of the flat slab at a nearly constant depth in the uppermost lower mantle. The possible topographic changes of the 810-km reflector may be caused by thermal and thickness variations of the oceanic plateau.

By comparing with seismic tomographic models and exploring all possible geodynamic and mineralogical explanations, we conclude that the 810-km reflector we observed most likely indicates a megameter-scale thickened crust subducted to the lower mantle. Because this thick crust is on the trajectory of the Hawaiian-Emperor seamount chain (Fig. 1), we propose that it is a major portion of the oceanic plateau associated with the head of the Hawaiian mantle plume. Because oceanic plateaus are small compared with the volume of global oceanic crust, the subduction of these plateaus will not bias our estimate of the mantle bulk composition. However, this process can lead to localized enrichment of basalt in the mantle and can locally alter the slab buoyancy, slowing down subduction (18) and contributing to the flattening of slabs above the 660-km discontinuity. If we assume a constant subduction rate of 75 mm/year and a slab dip angle of 50° above the flat part (38), this oceanic plateau subducted into the Kamchatka Trench ~20 to 30 Ma ago. The subduction of the oceanic plateau is apparently much younger than the bend of the Hawaiian-Emperor seamount chain and therefore not related to the change in the Pacific Plate motion ~47 Ma ago (5). Previous studies suggest that the collision between the Ontong Java Plateau and the northern Australian Plate margin 6 Ma ago caused a series of plate tectonic events,

including the counterclockwise rotation of the Pacific Plate (39). The subduction of this Hawaiian plume oceanic plateau temporally coincides with a kink of the Hawaiian-Emperor chain east of Midway Island. However, the causality is unclear, partially because the East Pacific Rise collided with the North American Plate around the same time. On the other hand, the subduction of the Pampean flat slab ~10 Ma ago did not cause any drastic plate reorganization. Further studies with more observations are needed to examine the relationship between oceanic plateau subduction and plate reorganization.

Plate reconstruction models using different mantle reference frames with moving hot spot frames suggest that the Hawaiian hot spot moved from the Izanagi Plate to the Pacific Plate ~100 Ma ago if the hot spot existed earlier (3, 4, 40, 41). If the Hawaiian plume head surfaced on the Izanagi Plate, the oceanic plateau would have been subducted into the Aleutian Trench toward the North Pole more than 70 Ma ago, which is inconsistent with our observation. Therefore, we believe that the oceanic plateau associated with the Hawaiian plume head was formed on the Pacific Plate no earlier than 106 Ma ago. This estimate is consistent with the 93-to 120-Ma-old ophiolitic basalts in Kamchatka that were produced by the Hawaiian plume and accreted to the Kamchatka forearc much later (14). Given the available plate reconstruction models (3, 4, 40, 41), we hypothesize that the Hawaiian plume head surfaced ~100 Ma ago to create a megameter-scale oceanic plateau at the Izanagi-Pacific Ridge (fig. S11). As the mid-ocean ridge spread, the oceanic plateau broke into two parts, and

the Izanagi part moved northward and subducted into the ancient Aleutian Trench ~72 Ma ago. On the other hand, before the Pacific part of the oceanic plateau subducted into the Kamchatka Trench, its eastern margin might also have encountered the Aleutian Trench and a possible subduction zone between the Kula and Kronos Plates (42). There are discrepancies between the plate reconstruction models and our inferences regarding the subduction time and the present position of the Pacific part of the oceanic plateau. This direct comparison is challenging because the detailed history of this plateau highly depends on the initial location and migration rate of the Izanagi-Pacific Ridge. However, our observations provide critical constraints for future plate reconstructions.

## REFERENCES AND NOTES

- J. T. Wilson, *Can. J. Phys.* **41**, 863–870 (1963).
- W. J. Morgan, *Nature* **230**, 42–43 (1971).
- K. J. Matthews et al., *Global Planet. Change* **146**, 226–250 (2016).
- T. H. Torsvik et al., *Geochim. Geophys. Geosyst.* **20**, 3659–3689 (2019).
- T. H. Torsvik et al., *Nat. Commun.* **8**, 15660 (2017).
- I. H. Campbell, R. W. Griffiths, *Earth Planet. Sci. Lett.* **99**, 79–93 (1990).
- S. E. Bryan, L. Ferrari, *Geol. Soc. Am. Bull.* **125**, 1053–1078 (2013).
- P. Glišović, A. M. Forte, *Science* **355**, 613–616 (2017).
- P. R. Vogt, *Nature* **241**, 189–191 (1973).
- G. P. Avdeiko, D. P. Savelyev, A. A. Palueva, S. V. Popruzherko, in *Volcanism and Subduction: The Kamchatka Region*, J. Eichelberger, E. Gordeev, P. Izbekov, M. Kasahara, J. Lees, Eds. (Geophysical Monograph Series, American Geophysical Union, 2007), pp. 37–55.
- R. A. Duncan, R. A. Keller, *Geochim. Geophys. Geosyst.* **5**, Q08L03 (2004).
- Y. L. Niu, M. J. O'Hara, J. A. Pearce, *J. Petrol.* **44**, 851–866 (2003).
- B. Steinberger, C. Gaina, *Geology* **35**, 407–410 (2007).
- M. Portnyagin, D. Savelyev, K. Hoernle, F. Hauff, D. Garbe-Schonberg, *Geology* **36**, 903–906 (2008).
- M. Cloos, *Geol. Soc. Am. Bull.* **105**, 715–737 (1993).
- G. Rossi, G. A. Abers, S. Rondenay, D. H. Christensen, *J. Geophys. Res. Solid Earth* **111**, B09311 (2006).
- C. R. Gans et al., *Geophys. J. Int.* **186**, 45–58 (2011).
- P.-A. Arrial, M. I. Billen, *Earth Planet. Sci. Lett.* **363**, 34–43 (2013).
- J. van Hunen, A. P. van den Berg, N. J. Vlaar, *Tectonophysics* **352**, 317–333 (2002).
- L. Liu et al., *Nat. Geosci.* **3**, 353–357 (2010).
- F. M. Dávila, C. Lithgow-Bertelloni, *Earth Planet. Sci. Lett.* **425**, 34–43 (2015).
- S. W. French, B. Romanowicz, *Nature* **525**, 95–99 (2015).
- C. Lu, S. P. Grand, H. Y. Lai, E. J. Garner, J. Geophys. Res. *Solid Earth* **124**, 11549–11567 (2019).
- J. M. Lees et al., in *Volcanism and Subduction: The Kamchatka Region*, J. Eichelberger, E. Gordeev, P. Izbekov, M. Kasahara, J. Lees, Eds. (Geophysical Monograph Series, American Geophysical Union, 2007), pp. 65–75.
- H. Kawakatsu, F. L. Niu, *Nature* **371**, 301–305 (1994).
- L. Waszek, N. C. Schmerr, M. D. Ballmer, *Nat. Commun.* **9**, 385 (2018).
- R. Maguire, J. Ritsema, S. Goes, *Geophys. Res. Lett.* **45**, 8913–8922 (2018).
- Materials and methods are available as supplementary materials.
- P. M. Shearer, *Geophys. J. Int.* **115**, 878–904 (1993).
- N. Schmerr, C. Thomas, *Earth Planet. Sci. Lett.* **311**, 101–111 (2011).
- Z. Zheng, B. Romanowicz, *Geophys. J. Int.* **191**, 1361–1373 (2012).
- L. Stixrude, C. Lithgow-Bertelloni, *Geophys. J. Int.* **184**, 1180–1213 (2011).
- L. Stixrude, C. Lithgow-Bertelloni, *Geophys. J. Int.* **162**, 610–632 (2005).
- W. B. Xu, C. Lithgow-Bertelloni, L. Stixrude, J. Ritsema, *Earth Planet. Sci. Lett.* **275**, 70–79 (2008).
- L. Stixrude, C. Lithgow-Bertelloni, *Annu. Rev. Earth Planet. Sci.* **40**, 569–595 (2012).
- W. P. Richardson, E. A. Okal, S. Van der Lee, *Phys. Earth Planet. Inter.* **118**, 29–51 (2000).
- P. E. van Keken, S. Karato, D. A. Yuen, *Geophys. Res. Lett.* **23**, 1821–1824 (1996).
- E. M. Syracuse, G. A. Abers, *Geochem. Geophys. Geosyst.* **7**, Q05017 (2006).
- P. Wessel, L. W. Kroenke, *J. Geophys. Res. Solid Earth* **105**, 28255–28277 (2000).
- R. D. Müller et al., *Annu. Rev. Earth Planet. Sci.* **44**, 107–138 (2016).
- P. V. Doubrovine, B. Steinberger, T. H. Torsvik, *J. Geophys. Res. Solid Earth* **117**, B09101 (2012).
- M. Domeier et al., *Sci. Adv.* **3**, eaao2303 (2017).
- W. H. F. Smith, D. T. Sandwell, *Science* **277**, 1956–1962 (1997).
- P. Bird, *Geochem. Geophys. Geosyst.* **4**, 1027 (2003).
- B. L. N. Kennett, E. R. Engdahl, R. Buland, *Geophys. J. Int.* **122**, 108–124 (1995).
- R. D. Müller et al., *Geochem. Geophys. Geosyst.* **19**, 2243–2261 (2018).
- National Research Institute for Earth Science and Disaster Resilience, F-net dataset (2019); <https://doi.org/10.17598/nied.0005>.

## ACKNOWLEDGMENTS

We thank L. Colli, S. Dorfman, M. J. Krawczynski, R. Maguire, A. McNamara, W. Panero, J. Wu, and X. Yue for constructive discussions and Y. Liu for valuable help using GPlates (46). Three anonymous reviewers provided helpful comments to improve the manuscript. We thank the 2019 Interior of the Earth Gordon Research Conference for providing opportunities of interdisciplinary collaboration. We also appreciate the free access to GPlates for plate reconstructions. Seismic data analysis was supported in part through computational resources and services provided by the Institute for Cyber-Enabled Research at Michigan State University. **Funding:** This work was made possible by NSF grants OCE-1842989 to S.S.W., EAR-1620251 to P.M.S., EAR-1900633 to C.L.-B., and EAR-1853388 to L.S. S.S.W. and

D.T. were also supported by the MSU Geological Sciences Endowment. C.L.-B. was further supported by the Louis B. and Martha B. Slichter Endowment for Geosciences. **Author contributions:** S.S.W., with the help of P.M.S. and D.T., analyzed the seismic data. C.L.-B. and L.S. conducted the thermodynamic simulations of mantle minerals. D.T. downloaded and maintained the seismic database. S.S.W. took the lead in writing the manuscript, and all authors discussed the results and edited the manuscript. **Competing interests:** The authors declare no competing interests. **Data and materials availability:** We use 1987–2018 data from the following seismic networks (abbreviations defined at [www.fdsn.org/networks/](http://www.fdsn.org/networks/)): AC, AE, AF, AI, AK, AT, AU, AV, BE, BL, BX, C1, CB, CD, CH, CCM, CN, CT, CU, CZ, DK, DR, DW, EI, G, GB, GE, GT, HL, HT, IC, II, IP, IU, JP, KN, KO, KP, KR, KS, KZ, LX, MC, MI, MM, MS, MX, MY, NA, ND, NJ, NO, NR, NU, OE, OV, PL, PM, PR, PS, RM, RV, S, SV, TA, TM, TR, TT, TW, UK, US, VE, WI, and WM. All raw seismic data are available at the Data Management Center of Incorporated Research Institutions for Seismology (<http://ds.iris.edu/ds/nodes/dmc/>). We also use 1995–2018 F-net data from Japan's National Research Institute for Earth Science and Disaster Resilience (47). The thermodynamic simulation package HeFESTo (32, 33) is available at <https://github.com/stixrude/HeFESToRepository>, and Table\_270914 in this GitHub repository includes all parameters used for the thermodynamic simulations. GPlates is available at [www.gplates.org](http://www.gplates.org).

## SUPPLEMENTARY MATERIALS

[science.sciencemag.org/content/370/6519/983/suppl/DC1](https://science.sciencemag.org/content/370/6519/983/suppl/DC1)  
Materials and Methods  
Figs. S1 to S12  
References (48–63)  
Movie S1  
27 May 2020; accepted 8 October 2020  
10.1126/science.abb0312

## DEVELOPMENTAL BIOLOGY

# Tissue topography steers migrating *Drosophila* border cells

Wei Dai<sup>1\*</sup>†, Xiaoran Guo<sup>1\*</sup>, Yuansheng Cao<sup>2</sup>, James A. Mondo<sup>1</sup>, Joseph P. Campanale<sup>1</sup>, Brandon J. Montell<sup>3</sup>, Haley Burrous<sup>1</sup>, Sebastian Streichan<sup>4</sup>, Nir Gov<sup>5</sup>, Wouter-Jan Rappel<sup>2</sup>, Denise J. Montell<sup>1†</sup>

Moving cells can sense and respond to physical features of the microenvironment; however, *in vivo*, the significance of tissue topography is mostly unknown. Here, we used *Drosophila* border cells, an established model for *in vivo* cell migration, to study how chemical and physical information influences path selection. Although chemical cues were thought to be sufficient, live imaging, genetics, modeling, and simulations show that microtopography is also important. Chemoattractants promote predominantly posterior movement, whereas tissue architecture presents orthogonal information, a path of least resistance concentrated near the center of the egg chamber. E-cadherin supplies a permissive haptotactic cue. Our results provide insight into how cells integrate and prioritize topographical, adhesive, and chemoattractant cues to choose one path among many.

**C**ell migrations are essential in development, homeostasis, and disease. Although chemoattractants and repellents have been extensively studied (1–3), physical features of the microenvironment may be equally important. Here, we used

*Drosophila* border cells as a model and uncovered a role for tissue topography in directional cell migration *in vivo*. Border cells are 6 to 10 follicle cells that migrate ~150 μm over 3 to 6 hours within ovarian egg chambers, which are composed of 15 nurse cells and one oocyte

<sup>1</sup>Department of Molecular, Cellular, and Developmental Biology, University of California, Santa Barbara, CA 93106, USA. <sup>2</sup>Department of Physics, University of California, San Diego, CA 92093, USA. <sup>3</sup>Independent researcher. <sup>4</sup>Department of Physics, University of California, Santa Barbara, CA 93106, USA. <sup>5</sup>Department of Chemical Physics, Weizmann Institute of Science, Rehovot, Israel.

\*These authors contributed equally to this work.

†Present address: Cardiovascular Medicine Division, Brigham and Women's Hospital, Harvard Medical School, Boston, MA 02115, USA.

Corresponding author. Email: dmontell@ucsb.edu

Copyright 2020 American Association for the Advancement of Science. All rights reserved.